https://doi.org/10.5194/egusphere-2026-6188
Preprint. Discussion started: 6 November 2026
© Author(s) 2026. CC BY 4.0 License.

Extreme Dust Intensity is Decoupled from Spring Dust Intensity in the Taklamakan Desert due to Different Low-level Winds

Chenglong Zhou[1,4], Qingzhe Zhu[2,3*], Ze Chen[1,4], Xinghua Yang[1,5], Ali Mamtimin[1,4], Fan Yang[1,4], Wen Huo[1,4], Yu Wang[1,4]

[1] Institute of Desert Meteorology, China Meteorological Administration/National Observation and Research Station of Desert Meteorology, Taklimakan Desert of Xinjiang/Taklimakan Desert Meteorology Field Experiment Station of China Meteorological Administration/Xinjiang Key Laboratory of Desert Meteorology and Sandstorm, Urumqi, 830002, China

[2] State Key Laboratory of Physical Oceanography, Ocean University of China, Qingdao, 266100, China

[3] Department of Marine Meteorology, College of Oceanic and Atmospheric Sciences, Ocean University of China, Qingdao, 266100, China

[4] Tazhong National Climate Observatory, Qiemo, 841999, China

[5] College of Geographical Sciences, Shanxi Normal University, Taiyuan, 030000, China

*Corresponding author: Qingzhe Zhu (zhuqingzhe@ouc.edu.cn)

https://doi.org/10.5194/egusphere-2026-6188
Preprint. Discussion started: 6 November 2026
© Author(s) 2026. CC BY 4.0 License.

Abstract

Extreme dust events (EDEs) are intensifying under climate change, causing serious environmental and ecological issues. However, the relationship between EDE intensity and seasonal dust intensity remains unclear, limiting the possibility of using seasonal dust activities to estimate EDE strength. Using two satellite observation datasets, we investigate the relationship between interannual variations of spring dust intensity and EDE intensity in North Africa (NA), the Middle East (ME), and the Taklamakan Desert (TD). Results reveal that EDE intensity strongly correlates with spring dust intensity on an interannual basis in NA and ME, whereas no significant correlation exists between them in TD. The discrepancy in TD arises because spring dust and EDEs are driven by different atmospheric circulations: spring dust responds to a "positive-negative-positive" geopotential pattern over Europe, Central Asia, and East Asia which caused by European precipitation anomalies; conversely, EDEs are linked to a negative geopotential height pattern over East Asia which is originated from the diabatic heating/cooling due to the western/eastern North Atlantic precipitation anomalies. A composite index, integrating spring and EDE circulations, can effectively characterize the dust intensity variation difference in TD. In the future, the inconsistency between the interannual variability of EDE intensity and that of spring dust intensity will persist under high-emission scenarios. Our study demonstrates EDEs in TD are relatively independent of spring dust activities, providing a novel framework for improving EDE predictability.

https://doi.org/10.5194/egusphere-2026-6188
Preprint. Discussion started: 6 November 2026
© Author(s) 2026. CC BY 4.0 License.

1. Introduction

The increasing frequency and intensity of extreme weather events under climate change have presented significant global challenges (Liao et al., 2021; Bevacqua et al., 2023; Lei et al., 2024). An extreme dust event (EDE) is a type of extreme weather event originating from desert regions, characterized by high dust intensity and extensive impact areas (Gui et al., 2022; Zhu and Liu, 2024). The impacts of dust aerosols from EDEs are multifaceted, mainly including affecting the global radiation budget through scattering and absorption, altering cloud microphysical processes by acting as cloud condensation and ice nuclei, and significantly impairing regional air quality and reducing visibility (Kawai et al., 2021; Mostamandi et al., 2023; Zamora and Kahn, 2024), which have a direct consequences for the regional economy, ecological environment, and human health (Cañadillas-Ramallo et al., 2022; Rodríguez and López-Darias, 2024).

Recent notable EDEs include the unprecedented trans-Atlantic African dust plume in June 2020 (Pu and Jin, 2021), which severely worsened air quality across the tropical North Atlantic and North America. In addition, a severe African dust event erupted from March 27 to April 01, 2024, with large masses of Saharan dust crossing the central Mediterranean and invading Europe, causing serious impacts on air quality, visibility, and human health in Italy, France, Switzerland, and Germany (Pons et al., 2025). East Asia has also seen intense EDEs in recent years, such as the March 2021 Gobi Desert storms which resulted in the strongest dust event in northern China in nearly a decade (Gui et al., 2022; Yin et al., 2022), and the persistent dust activities in spring 2023 which led to the highest frequency of dust events in China since 2011 (Chen et al., 2023; Chen et al., 2024). Moreover, EDEs also occur in the Middle East and India (Singh et al., 2021; Zittis et al., 2022).

Due to the low probability characteristic of EDEs, current EDE-related research primarily focuses on case studies similar to those mentioned above. Satellite observations provide robust support for identifying, tracking, and analyzing typical EDEs, deepening our understanding of their characteristics (Pu and Jin, 2021; Xue et al., 2025; Pons et al., 2025). However, due to the constraints of case studies, there remains a lack of analysis on the long-term evolution of EDEs, limiting our comprehension of their long-term features. Some polar-orbiting satellites possess global detection capabilities and decades of continuous observation records (such as Terra and Aqua), providing invaluable data for studying the long-term characteristics of dust activity and its relationship with climate change (Wei et al., 2024; Urraca et al., 2025). Currently, these long-term

https://doi.org/10.5194/egusphere-2026-6188
Preprint. Discussion started: 6 November 2026
© Author(s) 2026. CC BY 4.0 License.

aerosol observations are primarily used for analyzing interannual variations and trends in seasonal or annual average dust parameters (Gandham et al., 2022; Merdji et al., 2023). Against the backdrop of increasingly severe extreme weather events, investigating the long-term variability characteristics of EDEs is crucial. Furthermore, the low probability of extreme weather events also makes their frequency and intensity difficult to predict, while forecasts for seasonal averaged patterns of meteorological elements are relatively accurate at present (Devanand et al., 2024; Doi et al., 2024; Wu et al., 2025). Therefore, clarifying the relationship between the interannual variation in EDE intensity and the interannual variation in seasonal dust intensity is crucial for predicting the EDE strength. Critically, if EDE intensity is not strongly tied to seasonal dust intensity, predicting these extreme events based on seasonal forecasts becomes vastly more challenging.

To address the above issues, we utilized multi-source satellite observations to obtain the long-term characteristics of dust aerosol optical depth (DOD) during EDEs and spring in global major dust regions to assess dust intensity. In addition, we compared the relationship between interannual variations of EDE DOD and those of spring DOD, as well as analyzed the reasons for the differences in their interannual variations. Furthermore, an index for the interannual differences between EDE DOD and spring DOD was provided. Finally, the relative independence of EDE DOD relative to spring DOD was discussed, future changes were briefly analyzed, and potential uncertainties were clarified. Our findings indicate that EDE intensity is decoupled from spring dust intensity in the Taklamakan Desert, and EDE DOD is relatively independent of spring DOD, rather than a simple amplification of the spring dust activity. The results of this study will improve the understanding of long-term variations in the EDE intensity, promote awareness of the unique features of EDEs, and provide assistance for future EDE predictions.

2. Data and Methods

2.1. Satellite-based aerosol products

In this study, the daily aerosol optical depth (AOD) at 550 nm, Ångström exponent (AE) at 412-470 nm, and single scattering albedo (SSA) at 470 nm derived from the Terra MODIS Collection 6.1 level 2 products (MOD04_L2) during the spring from 2000 to 2025 were used to calculate the daily DOD. These variables are given by the latest Deep Blue algorithm, which

https://doi.org/10.5194/egusphere-2026-6188
Preprint. Discussion started: 6 November 2026
© Author(s) 2026. CC BY 4.0 License.

consists of geolocated granules of 10 × 10 pixels, each with a 1 km resolution at nadir. Only quality-assured (QA = 1) data were selected for analysis.

DOD in this study is mainly calculated based on Pu and Ginoux (2018). The calculation formula is as follows:

$$DOD = AOD_{550nm} \times (0.98 - 0.508 \times AE + 0.051 \times AE^2) \quad (1)$$

This method requires SSA at 470 nm to be less than 0.99 for the retrieval of DOD.

Moreover, Li and Ginoux (2025) recently released an updated DOD inversion algorithm. The calculation formula is as follows:

$$DOD = AOD_{550nm} \times [1 - (0.051 + 0.336 \times AE + 0.085 \times AE^2)] \quad (2)$$

To avoid uncertainty caused by a single algorithm, the method by Li and Ginoux (2025) has also been applied to the calculation of DOD. The calculated DOD by each algorithm is interpolated to a grid of 1° × 1°.

In addition, the infrared atmospheric sounder interferometer (IASI) launched onboard the European Meteorological Operational satellite (METOP) directly provides the DOD observation from 2008 to 2023, showing high quality in capturing the spatiotemporal variability of dust in comparison to ground measurements (Blumstein et al., 2004; Capelle et al., 2018). In this study, daily gridded DOD at 10 μm with a resolution of 1° during the spring from 2008 to 2023 was used, and the DOD product is derived from the average of an ensemble of multiple algorithms.

2.2. Meteorological products

The hourly meteorological conditions including 10-m winds (UV10), soil water (SW), precipitation (P), potential evaporation (PE), winds at 850 hPa (UV850) derived from ERA5 reanalysis datasets (Hersbach et al., 2020) with a resolution of 0.5° and the daily Normalized Difference Vegetation Index (NDVI) observed by Advanced Very High Resolution Radiometer (AVHRR) from NOAA Climate Data Records with a resolution of 0.05° were used to assess the impact of meteorological conditions on DOD variations. The hourly geopotential height at 500 hPa (G500) derived from ERA5 was used for the calculation of Rossby wave activity flux (Takaya and Nakamura, 2001), and the hourly air temperature, vertical velocity, and horizontal wind vector between 850 hPa and 300 hPa derived from ERA5 were used for the calculation of the apparent heat source (Yanai et al., 1973).

https://doi.org/10.5194/egusphere-2026-6188
Preprint. Discussion started: 6 November 2026
© Author(s) 2026. CC BY 4.0 License.

2.3. CMIP6 model

The daily AOD datasets under the first variant level "r1i1p1f1" were obtained from CMIP6. The historical experiments and two Shared Socioeconomic Pathways (SSPs) scenario experiments were used (SSP245 and SSP585). According to the availability of predictors, 5 models including AWI-ESM-1-REcoM, MPI-ESM1-2-HR, MPI-ESM1-2-LR, NorESM2-LM, and UKESM1-0 were selected.

3. Methods

3.1. Identification of extreme dust events

An extreme dust day was defined as a day where the regionally averaged daily DOD exceeded the 90th percentile of all spring daily DOD values during the study period (2000-2025 for MODIS, 2008-2023 for IASI). Furthermore, extreme dust days were also extracted at the 85th percentile to avoid uncertainty associated with a single threshold. For each year, DODs during all extreme dust days were averaged to calculate the annual EDE DOD, which represents the EDE intensity, and spring DOD was calculated by the seasonal mean (March-April-May) of daily regional average DOD to characterize the spring dust intensity.

3.2. Linear Baroclinic Model

To reveal the effect of diabatic heating/cooling on 10-m winds, a linear baroclinic model (LBM), which can elucidate complex feedback in the atmosphere, was used in this study (Watanabe and Kimoto, 2000). The model was derived from the NCEP reanalysis and operated at a horizontal resolution of 2.8° × 2.8° and 20 vertical levels in the sigma coordinate. The LBM has been widely used to study atmospheric responses under given heating conditions (An et al., 2023; Fu et al., 2024; Huang et al., 2024). In this study, the horizontal ellipse shape and the vertical sine function are used to generate the forcing, with the default diffusion and damping coefficients. The maximum heating rate is applied at 0.5 of the sigma layers (about 500 hPa), and the integration time of the model is set to 20 days.

3.3. Statistical analysis

Pearson correlation, regression analysis, and the two-tailed Student's t test were applied to examine the relationship between EDE DOD and spring DOD. An empirical orthogonal function (EOF) analysis was used to obtain the dominant modes of EDE DOD and spring DOD.

https://doi.org/10.5194/egusphere-2026-6188
Preprint. Discussion started: 6 November 2026
© Author(s) 2026. CC BY 4.0 License.

4. Results

4.1. Regional differences in the correlation between EDE intensity and spring dust intensity

The spatial distributions of the spring DOD derived from IASI (Fig. 1a) and MODIS using the Pu and Ginoux (2018) algorithm (Fig. 1c) indicate that spring dusts are mainly distributed in the mid-to-low latitude regions from Africa to East Asia, with North Africa (NA), the Middle East (ME), and the Taklamakan Desert (TD) being the global main high-value areas for DOD. Fig. 1b shows the daily regional average DOD derived from IASI in NA, ME, and TD during the spring of 2008-2023, and the orange dots represent the 90th percentile of daily DOD, which is the threshold for EDE. Similarly, characteristics of DOD derived from MODIS during the spring of 2000-2025 (Fig. 1d) are consistent with those derived from IASI.

Based on MODIS daily DOD by Pu and Ginoux (2018) algorithm and corresponding EDE thresholds, the interannual variations of spring DOD and EDE DOD in NA, ME, and TD from 2000 to 2025 are characterized (Figs. 2a1-a3). Both the spring DOD and EDE DOD in NA and those in ME first increase and then decrease (Figs. 2a1-a2). Spring DOD and EDE DOD in TD both show a decreasing trend and exhibit strong interannual variability (Fig. 2a3). As depicted in Figs. 2b1 and 2b2, the interannual variations of spring DOD and EDE DOD in NA and ME show great consistency, with correlation coefficients of 0.35 and 0.42, respectively, both significant at a 90% confidence level ($p < 0.1$). However, the correlation between the two metrics in TD is weak and insignificant (Fig. 2b3). The MODIS DOD results obtained using the Li and Ginoux (2025) algorithm (Figs. 2c1-d3) and the results derived from IASI (Figs. 3a1-b3) confirmed the robustness of the above phenomenon.

To avoid uncertainty caused by a single EDE threshold, Fig. 3c shows the results of using the 85th percentile of daily DOD as the EDE threshold. Similar to the results obtained when the 90th percentile was used as the EDE threshold, the relationship between spring DOD and EDE DOD in TD remained weak and insignificant when the threshold was lowered (purple bars in Fig. 3c); even results based on IASI indicate a weak negative correlation between spring DOD and EDE DOD. In addition, there is still a strong positive correlation between spring DOD and EDE DOD in NA and ME. These results clearly indicate the uniqueness of EDE DOD in TD compared to EDE DOD in NA and ME, which shows that there is no obvious relationship between EDE DOD and spring DOD in TD.

https://doi.org/10.5194/egusphere-2026-6188
Preprint. Discussion started: 6 November 2026
© Author(s) 2026. CC BY 4.0 License.

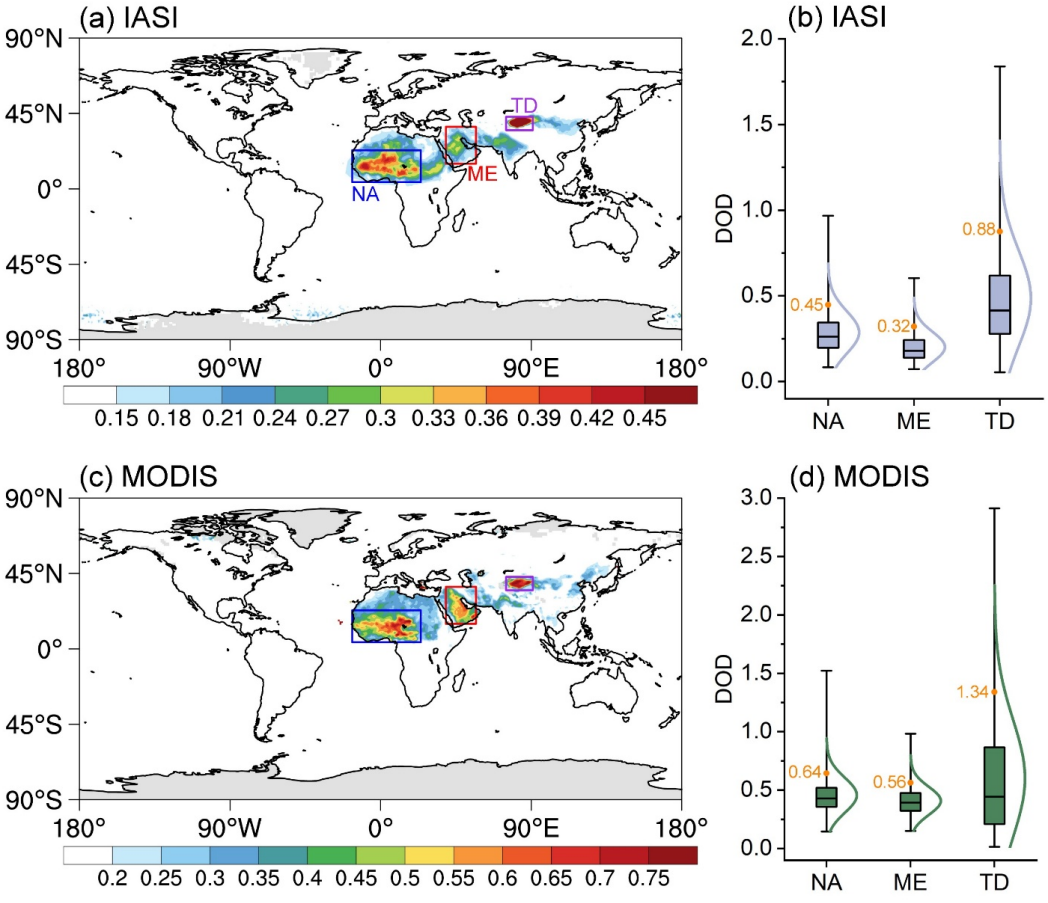


Figure 1. (a) Spatial distributions of the spring DOD at 10 μm derived from IASI during 2008-2023. The blue, red, and purple rectangles represent NA (4-23°N, 17°W-24°E), ME (15-37°N, 39-57°E), and TD (the area below 2000 m within 36-43°N, 75-90°E), respectively. (b) Box plots of the daily regional averaged DOD derived from IASI during the spring of 2008-2023 in NA, ME, and TD. The 90th percentile of daily DOD is marked in the orange point; the value on the left side of the point is the corresponding DOD value. Boxes show medians and 25-75% interquartile ranges; whiskers present minimum-maximum ranges. Curves represent the normal distributions of daily DOD. (c) and (d) same as in (a) and (b), but for spring DOD at 550 nm derived from MODIS using the Pu and Ginoux (2018) algorithm during 2000-2025.

https://doi.org/10.5194/egusphere-2026-6188
Preprint. Discussion started: 6 November 2026
© Author(s) 2026. CC BY 4.0 License.

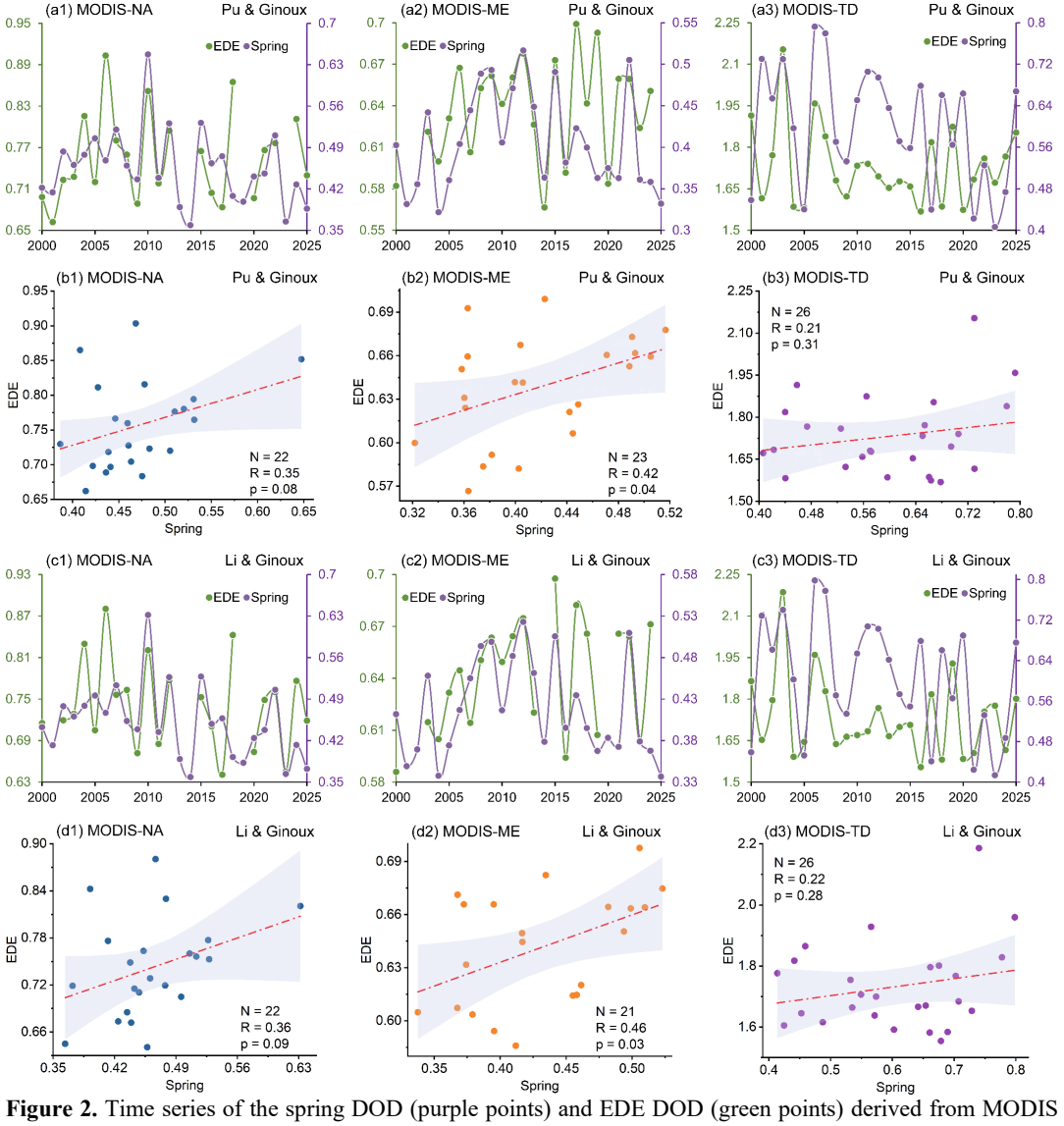


Figure 2. Time series of the spring DOD (purple points) and EDE DOD (green points) derived from MODIS using the Pu and Ginoux (2018) algorithm during 2000-2025 in (a1) NA, (a2) ME, and (a3) TD. The missing points indicate no EDEs occurred in the year. Scatter plots of spring DOD (horizontal axis) and EDE DOD (vertical axis) derived from MODIS during 2000-2025 in (b1) NA, (b2) ME, and (b3) TD. (c1-c3) same as in (a1-a3), and (d1-d3) same as in (b1-b3), but for MODIS using the Li and Ginoux (2025) algorithm. Red dashed lines in (b1-b3) and (d1-d3) represent the linear fits, and corresponding 95% confidence intervals are represented by shaded areas. N, R, and p indicate the sample size, linear correlation coefficient, and probability value (p-value), respectively.

https://doi.org/10.5194/egusphere-2026-6188
Preprint. Discussion started: 6 November 2026
© Author(s) 2026. CC BY 4.0 License.

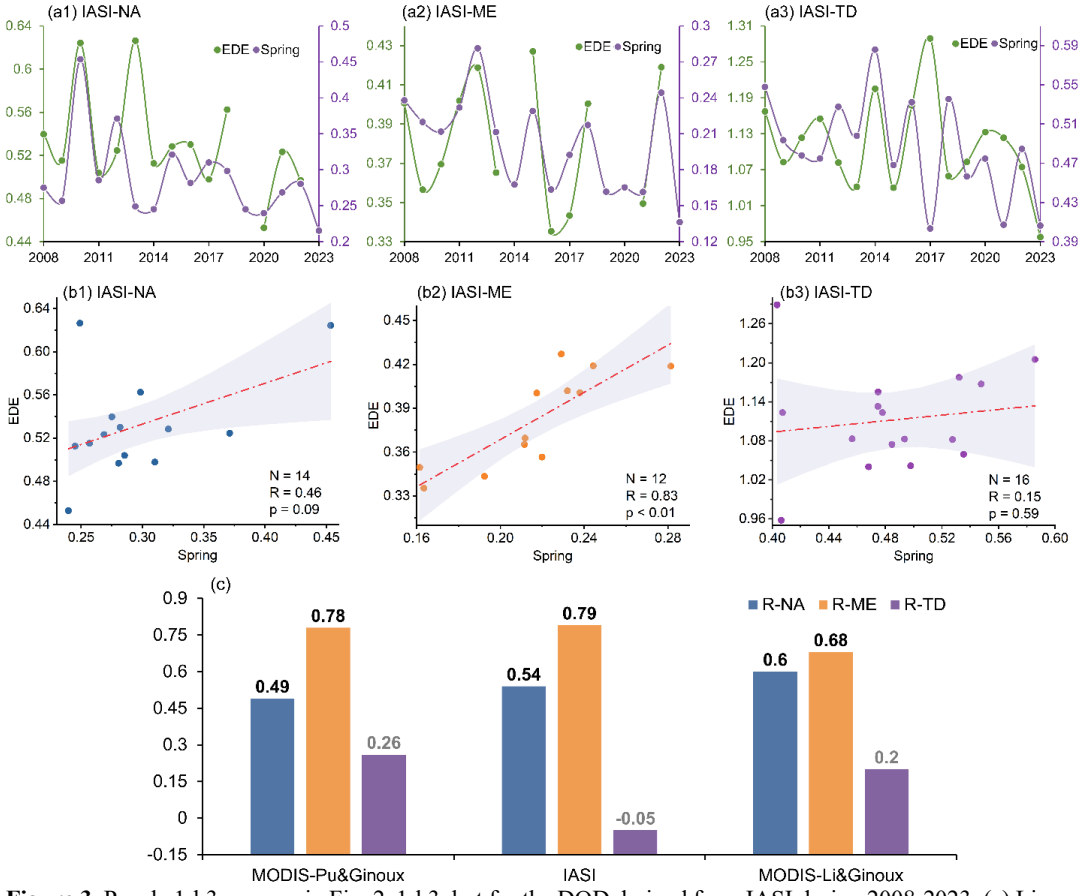


Figure 3. Panel a1-b3 same as in Fig. 2a1-b3, but for the DOD derived from IASI during 2008-2023. (c) Linear correlation coefficients between spring DOD and EDE DOD calculated based on the 85th percentile in NA (blue bars), ME (yellow bars), and TD (purple bars). Black numbers indicate the correlation coefficients are significant at the 90% confidence level; gray numbers indicate the correlation coefficients are insignificant at the 90% confidence level.

4.2. The inconsistent interannual variability of spring dust intensity and extreme dust intensity in TD

MODIS delivers longer-term aerosol records relative to IASI aerosol observations, and the results derived from both datasets are in good agreement. Since the algorithm developed by Pu and Ginoux (2018) has undergone far more comprehensive validation than the Li and Ginoux (2025) algorithm, all subsequent analyses rely on DOD retrievals from MODIS using the Pu and Ginoux (2018) algorithm. The spatial distributions of spring DOD and EDE DOD in TD during 2000-2025 are presented in Fig. 4a and Fig. 4b, implying the difference in the spatial distribution of spring DOD and EDE DOD, which is manifested by the high-value areas of spring DOD being mainly

https://doi.org/10.5194/egusphere-2026-6188
Preprint. Discussion started: 6 November 2026
© Author(s) 2026. CC BY 4.0 License.

distributed in the northern TD, while the high-value area of EDE DOD is distributed in the central TD. Based on the time series of spring DOD and EDE DOD, the corresponding time series of DOD anomalies are obtained (Fig. 4c). In some years, the variations of spring DOD and EDE DOD are consistent, while in other years there are opposite changes. The magnitude of the difference between the spring DOD anomalies and EDE DOD anomalies (Fig. 4d) characterizes the difference between the interannual variation of spring DOD and that of EDE DOD. The red bars in Fig. 4d present the anomaly differences are higher than the average difference, and the blue bars present the anomaly differences are lower than the average difference. Spring DOD and EDE DOD are strongly correlated in years with small anomaly differences (Fig. 4e), but weakly correlated when anomaly differences are large (Fig. 4f). Therefore, the magnitude of the DOD anomaly difference can characterize the consistency of interannual variations of spring DOD and EDE DOD: small anomaly differences indicate high consistency between their interannual variations.

https://doi.org/10.5194/egusphere-2026-6188
Preprint. Discussion started: 6 November 2026
© Author(s) 2026. CC BY 4.0 License.

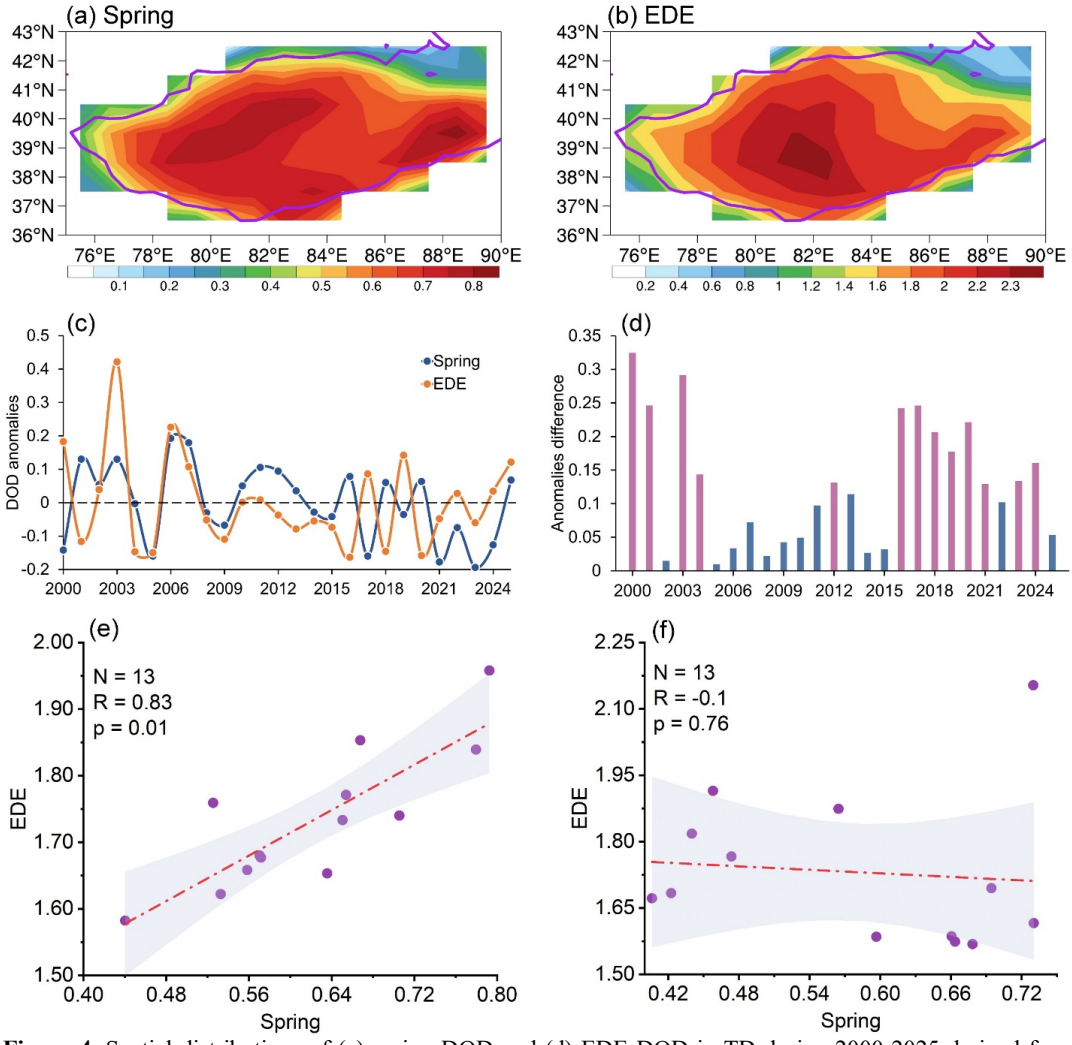


Figure 4. Spatial distributions of (a) spring DOD and (d) EDE DOD in TD during 2000-2025 derived from MODIS observations. The purple solid curve denotes the topographic contour line of 2000 m, representing the TD domain. (c) Time series of the spring DOD anomalies (blue points) and EDE DOD anomalies (orange points) in TD during 2000-2025. (d) Time series of the magnitude of the DOD anomaly differences between spring and EDEs; the red bars represent the anomaly differences are higher than the average difference, and the blue bars represent the anomaly differences are lower than the average difference. Scatter plots of spring DOD (horizontal axis) and EDE DOD (vertical axis) in TD (e) during the years with low anomaly differences (the years corresponding to the blue bars in panel d) and (f) during the years with high anomaly differences (the years corresponding to the red bars in panel d).

Due to their low probability of occurrence, extreme weather events are difficult to predict, and the weak correlation between interannual variations of EDE DOD and spring DOD further increases the difficulty of predicting the intensity of EDE in TD. Therefore, the factors influencing

https://doi.org/10.5194/egusphere-2026-6188
Preprint. Discussion started: 6 November 2026
© Author(s) 2026. CC BY 4.0 License.

the inconsistency between interannual variations of EDE DOD and spring DOD in TD are further analyzed. As reported by previous studies, strong winds during dust events and surface droughts prior to dust events are key factors influencing dust events (Yin et al., 2022; Zhu and Liu, 2024; Mu and Fiedler, 2025). Therefore, the difference between the EDE period low-level wind speed and spring low-level wind speed (UV10 and UV850), as well as the difference between pre-EDE period surface characteristics and spring surface characteristics (SW, P, NDVI, and PE) in TD were calculated. Fig. 5a shows the correlation coefficients between the EDE-spring differences in the above variables and the EDE-spring DOD differences, revealing differences in low-level winds and SW are significantly correlated with DOD differences. Specifically, stronger wind differences (EDE relative to spring) and lower SW differences (pre-EDE relative to spring) correspond to greater EDE-spring DOD differences (Fig. 5a).

The above results indicate that stronger winds and more severe droughts lead to stronger DOD, with low-level wind speed and SW being the key factors influencing the EDE-spring DOD differences. However, only the interannual variation of EDE low-level winds is weakly correlated with that of spring low-level winds; the interannual variation of SW before EDEs is strongly correlated with that of spring SW (Fig. 5b). Therefore, low-level winds and SW jointly dominate the EDE-spring DOD differences, while the interannual decoupling between EDE DOD and spring DOD is attributed to the inconsistent interannual variations of low-level winds between EDE and spring.

https://doi.org/10.5194/egusphere-2026-6188
Preprint. Discussion started: 6 November 2026
© Author(s) 2026. CC BY 4.0 License.

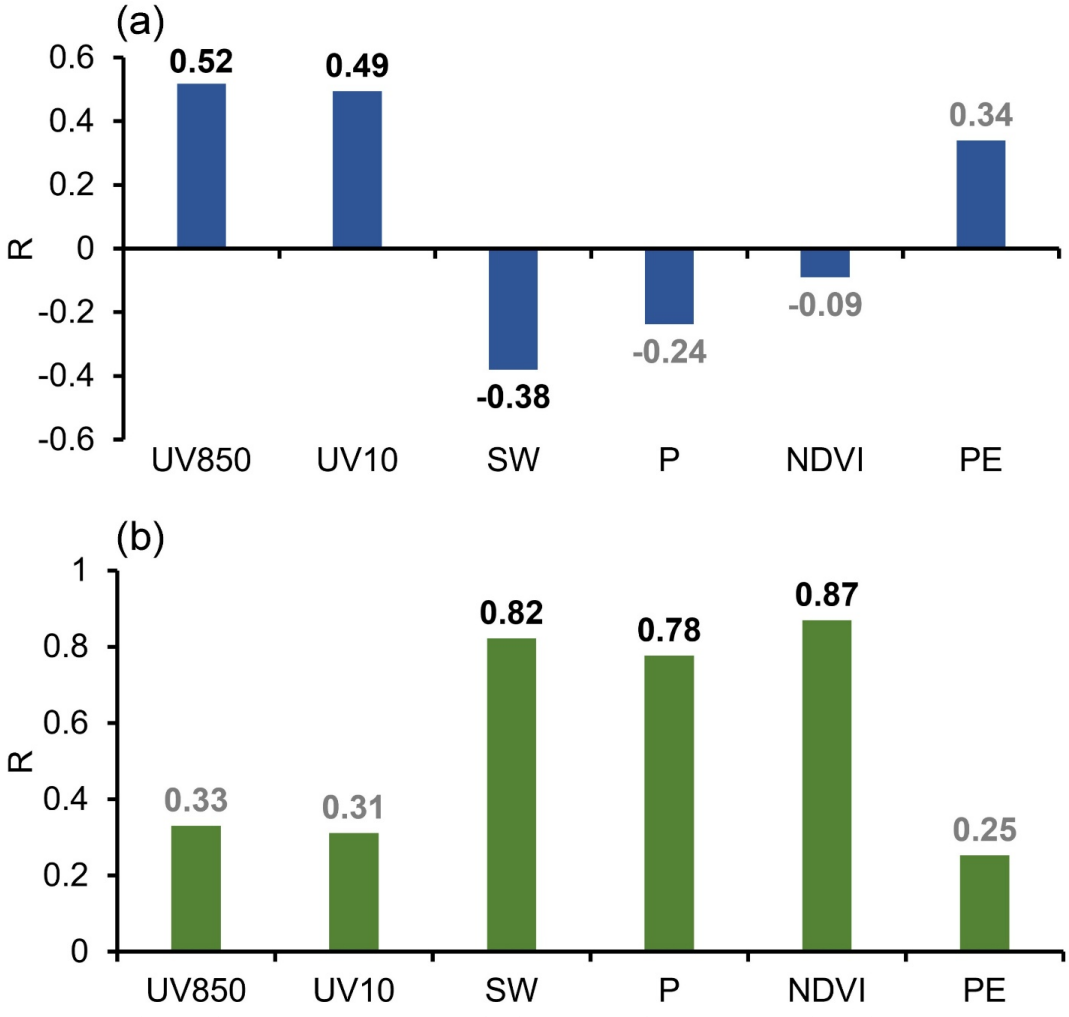


Figure 5. (a) The correlation coefficients between the difference of the low-level wind speed (UV10 and UV850) during EDE and spring low-level wind speed and the difference of the EDE DOD and spring DOD in TD from 2000-2025, as well as the correlation coefficients between the difference of surface characteristics (SW, P, NDVI and PE) before EDE and spring surface characteristics and the difference of the EDE DOD and spring DOD in TD from 2000-2025. (b) The correlation coefficients between the low-level wind speed (UV10 and UV850) during EDE and spring low-level wind speed, as well as the correlation coefficients between the surface characteristics (SW, P, NDVI, and PE) before EDE and spring surface characteristics in TD from 2000-2025. Black numbers indicate the correlation coefficients are significant at the 95% confidence level; gray numbers indicate the correlation coefficients are insignificant at the 95% confidence level.

Regression analyses between the time series of spring UV10 in TD and spring G500, as well as those between the time series of EDE UV10 in TD and EDE G500 from 2000 to 2025, indicate that large-scale circulation systems affecting the spring UV10 and EDE UV10 are completely different (Figs. 6a and 6c). The “positive-negative-positive” pattern of the abnormal G500 over

https://doi.org/10.5194/egusphere-2026-6188
Preprint. Discussion started: 6 November 2026
© Author(s) 2026. CC BY 4.0 License.

Europe, Central Asia, and East Asia dominates the interannual variation of spring UV10 in TD (Fig. 6a), and the corresponding Rossby wave propagates from Northern Europe to TD. However, the interannual variation of EDE UV10 in TD is controlled by opposite G500 anomalies in the eastern and western North Atlantic (Fig. 6c), the corresponding Rossby wave propagates from the northwest Atlantic to the northeast Atlantic, then continues eastward along the north and south jets, ultimately converging in TD and surrounding areas (Fig. 6c). Based on the regression patterns of G500 onto the interannual variations of UV10, the geopotential height indexes (G-indexes) in spring and EDEs are established based on the prominent areas of the G500 regression patterns (purple rectangles in Figs. 6a and 6c). As depicted in Figs. 6b and 6d, the G-indexes can effectively reflect the interannual variations of spring UV10 and EDE UV10, with correlation coefficients of -0.56.

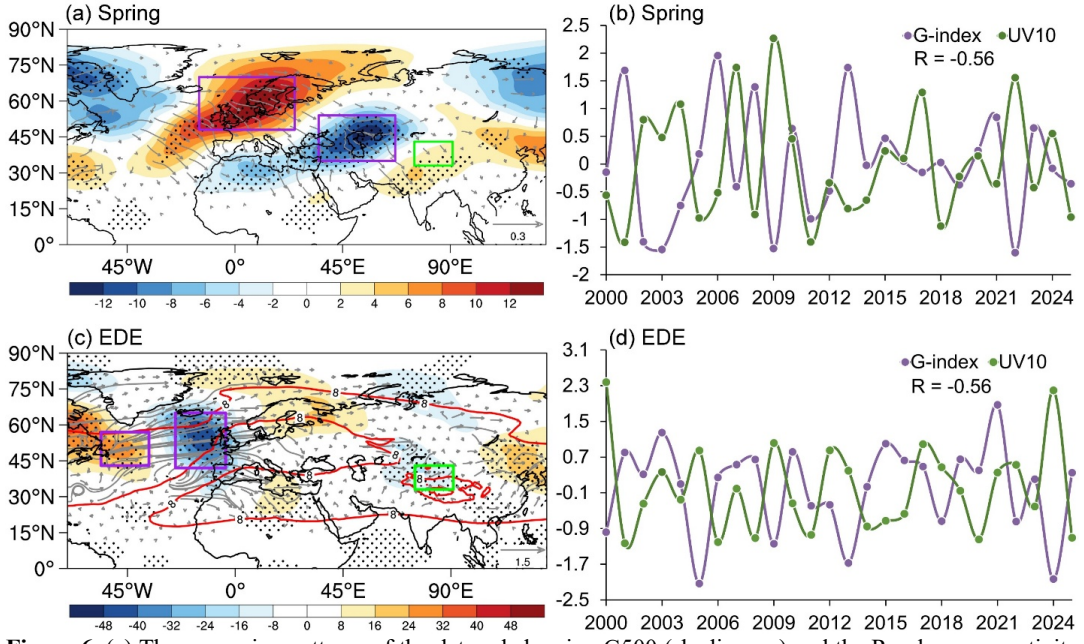


Figure 6. (a) The regression patterns of the detrended spring G500 (shading; m) and the Rossby wave activity flux at 500 hPa (vectors; $m^2\ s^{-2}$) onto detrended time series of spring UV10 in TD during 2000-2025. The purple rectangles represent the areas used to calculate the G-index. (b) Time series of detrended spring UV10 in TD (green points) and detrended spring G-index during 2000-2025. Spring G-index is obtained from the standardized difference between the spring G500 of the right rectangle and the spring G500 of the left rectangle in (a) from 2000 to 2025. (c) and (d) same as in (a) and (b), but for the EDE period. The red contours in (c) represent the averaged 500 hPa zonal winds is 8 m s^{-1} during all EDEs. EDE G-index is obtained from the standardized difference between the EDE G500 of the left rectangle and the EDE G500 of the right rectangle in (c) from 2000 to 2025. The dots in (a) and (c) represent the regression coefficients are significant above the 95% confidence level. The green rectangle in (a) and (c) represents TD. The linear correlation coefficients in (b) and (d) are indicated by R, which is significant at the 95% confidence level.

https://doi.org/10.5194/egusphere-2026-6188
Preprint. Discussion started: 6 November 2026
© Author(s) 2026. CC BY 4.0 License.

Anomalies in regional geopotential height are typically associated with diabatic heating or cooling caused by local precipitation anomalies (Kataoka et al., 2018; Shi et al., 2024). Figs.7a and 7b present anomalous precipitation distributions in spring and EDEs related to the G-index, indicating the G500 anomalies associated with spring UV10 are caused by abnormal heavy precipitation in Europe (Fig. 7a), while the G500 anomalies associated with EDE UV10 are caused by abnormal heavy precipitation in the eastern North Atlantic and abnormal less precipitation in the western North Atlantic (Fig. 7b). Correspondingly, diabatic heating associated with spring G500 anomalies occurs in Europe (Fig. 7c), while diabatic heating and diabatic cooling associated with EDE G500 anomalies occur in the eastern and western North Atlantic, respectively (Fig. 7d). Furthermore, there is a good spatial correspondence between abnormal G500, abnormal precipitation, and abnormal diabatic heating (Fig. 6 and Fig. 7).

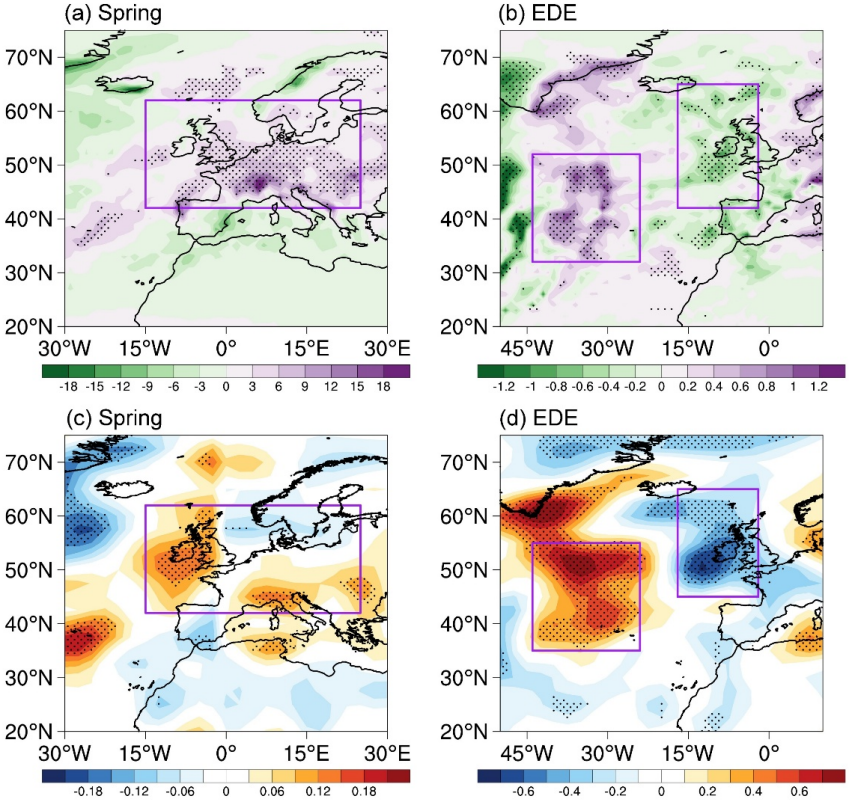


Figure 7. (a) The regression patterns of the detrended spring precipitation (mm day^{-1}) onto the detrended time series of spring G-index during 2000-2025. (b) Same as in (a), but for the EDE period. (c) The regression patterns of the detrended spring diabatic heating (K day^{-1}) onto the detrended time series of spring G-index during 2000-2025. (d) Same as in (c), but for the EDE period. The dots represent the regression coefficients are significant above the 95% confidence level.

https://doi.org/10.5194/egusphere-2026-6188
Preprint. Discussion started: 6 November 2026
© Author(s) 2026. CC BY 4.0 License.

To verify the role of Europe and the North Atlantic region in triggering spring UV10 and EDE UV10, we applied anomalous heating/cooling to the spring and the EDE atmospheric circulations during 2000-2025 in the LBM. During the 4-7 days when the spring anomalous heating was applied (shaded areas in Fig. 8a), abnormal high pressure (blue solid lines in Fig. 8a) and abnormal low pressure (blue dashed lines in Fig. 8a) appeared in Europe and Central Asia, respectively, with Rossby waves (purple arrows in Fig. 8a) propagating eastward from Europe. As the integration time increases, a "positive-negative-positive" G500 abnormal pattern across Europe, Central Asia, and East Asia, the corresponding Rossby wave propagated from Northern Europe to TD (Fig. 8b), which is consistent with the G500 corresponding to the spring UV10 (Fig. 6a). Therefore, the diabatic heating caused by increased spring precipitation in Europe does indeed affect the spring UV10 associated with spring DOD through the propagation of Rossby waves.

For the EDE period, when abnormal heating and abnormal cooling were applied to the western and eastern parts of the North Atlantic, respectively, Rossby waves propagated eastward from the North Atlantic and were divided into two branches: one propagating through Eurasia and the other through North Africa (Fig. 8c). With longer model integration, the Rossby waves converged in East Asia, causing abnormal low pressure to form in TD and surrounding areas (Fig. 8d), which has a great agreement with the G500 corresponding to the EDE UV10 (Fig. 6c). Consequently, the diabatic heating and diabatic cooling caused by abnormal precipitation in the western and eastern North Atlantic derived the EDE UV10 anomalies associated with EDE DOD by triggering abnormal geopotential height.

https://doi.org/10.5194/egusphere-2026-6188
Preprint. Discussion started: 6 November 2026
© Author(s) 2026. CC BY 4.0 License.

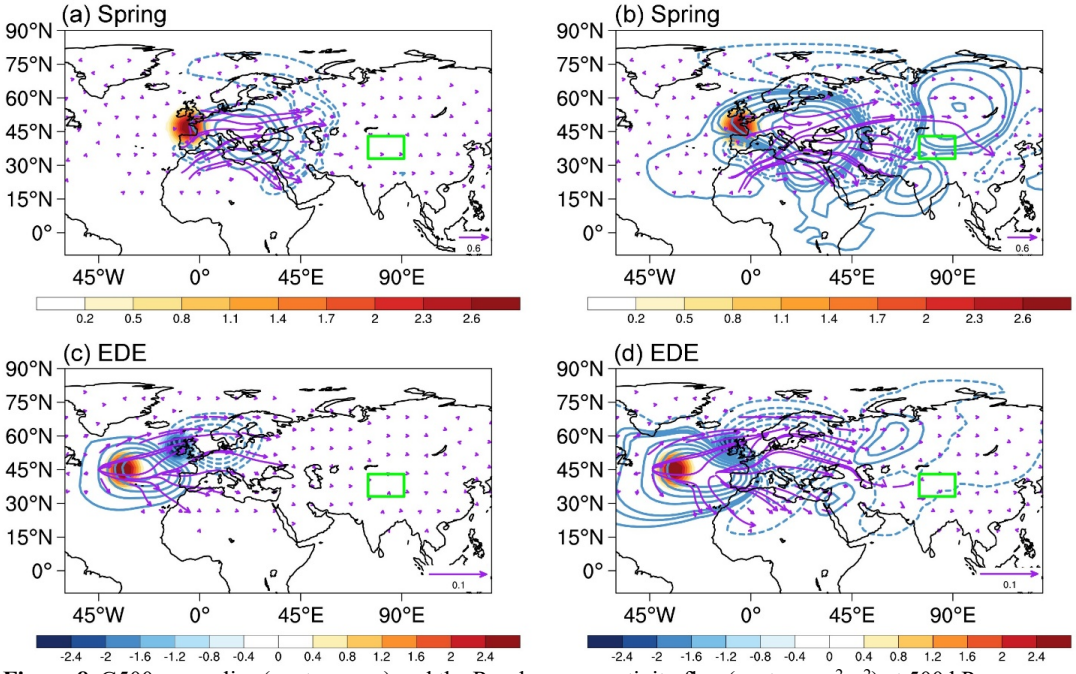


Figure 8. G500 anomalies (contours; m) and the Rossby wave activity flux (vectors; $m^2\ s^{-2}$) at 500 hPa response to the spring diabatic heating (shading; K day^{-1}) during the integration of (a) 4-7 days and (b) 7-9 days. G500 anomalies (contours; m) and the Rossby wave activity flux (vectors; $m^2\ s^{-2}$) at 500 hPa response to the EDE diabatic heating and diabatic cooling (shading; K day^{-1}) during the integration of (c) 2-3 days and (d) 4-5 days. The green rectangle represents TD. Blue solid contour lines represent abnormal high pressure, while dashed contour lines represent abnormal low pressure.

The above results indicate that different G500 anomalies drive the difference between spring UV10 and EDE UV10, which in turn causes inconsistent interannual variations in spring DOD and EDE DOD. As depicted in Fig. 4, the magnitude of the difference between the spring DOD anomalies and EDE DOD anomalies characterizes the difference between the interannual variation of spring DOD and that of EDE DOD. Therefore, we further combine the spring G-index and EDE G-index to characterize the difference in magnitude between spring DOD anomalies and EDE DOD anomalies. The purple points in Fig. 9 are the combined spring G-index and EDE G-index (Gc-index) obtained from multiple linear regression, which can accurately reproduce the interannual variation of DOD anomaly differences (the green points in Fig. 9). Therefore, the interannual variation difference between EDE DOD and spring DOD can be jointly characterized by spring G-index and EDE G-index, which can provide a reference for EDE intensity prediction.

https://doi.org/10.5194/egusphere-2026-6188
Preprint. Discussion started: 6 November 2026
© Author(s) 2026. CC BY 4.0 License.

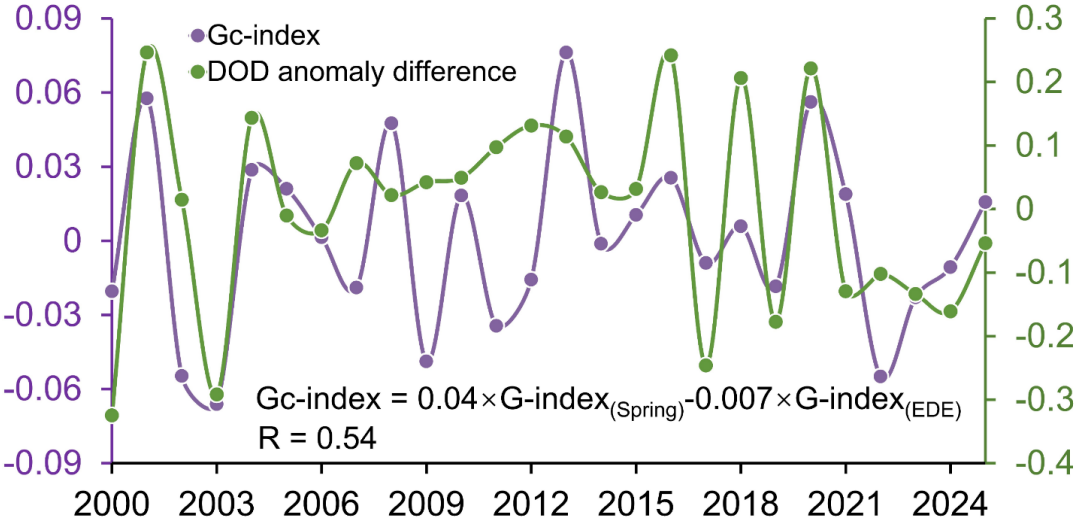


Figure 9. Time series of Gc-index anomalies (purple points) and the standardized magnitude of the difference between the spring DOD anomalies and EDE DOD anomalies (green points) during 2000-2025. The linear correlation coefficient is indicated by R, which is significant at the 95% confidence level.

In addition, using satellite observations, the relative independence of spring DOD and EDE DOD in TD is further analyzed. Fig. 10 presents the results of the EOF analysis of DOD during spring and EDEs derived from MODIS. The first EOF mode (EOF1) of spring DOD (Fig. 10a) is close to the spatial distribution of spring-averaged DOD (Fig. 4a), implying spring-averaged DOD shows consistent spatial variation throughout TD. The second EOF mode (EOF2) and the third EOF mode (EOF3) indicate that the spring DOD in TD shows north-south and east-west opposite spatial variations, respectively (Figs. 10b and 10c). The EOF1 of EDE DOD implies that the EDE DOD in TD shows east-west opposite spatial variations during 2000-2025 (Fig. 10d), which is consistent with the EOF3 of spring DOD (Fig. 10c) but completely different from the EOF1 of spring DOD which represents the spring-averaged DOD. Furthermore, the EOF analysis of DOD derived from IASI also indicates that the EOF1 of EDE DOD is consistent with the EOF2 of spring DOD (Figs. 11b and 11d), but completely unrelated to the EOF1 of spring DOD (Fig. 11a). Since the spatial modes obtained from the EOF analysis for spring DOD are independent of each other, the spatiotemporal distributions of spring-averaged DOD and EDE DOD are independent, which promotes inconsistencies in their interannual variations.

https://doi.org/10.5194/egusphere-2026-6188
Preprint. Discussion started: 6 November 2026
© Author(s) 2026. CC BY 4.0 License.

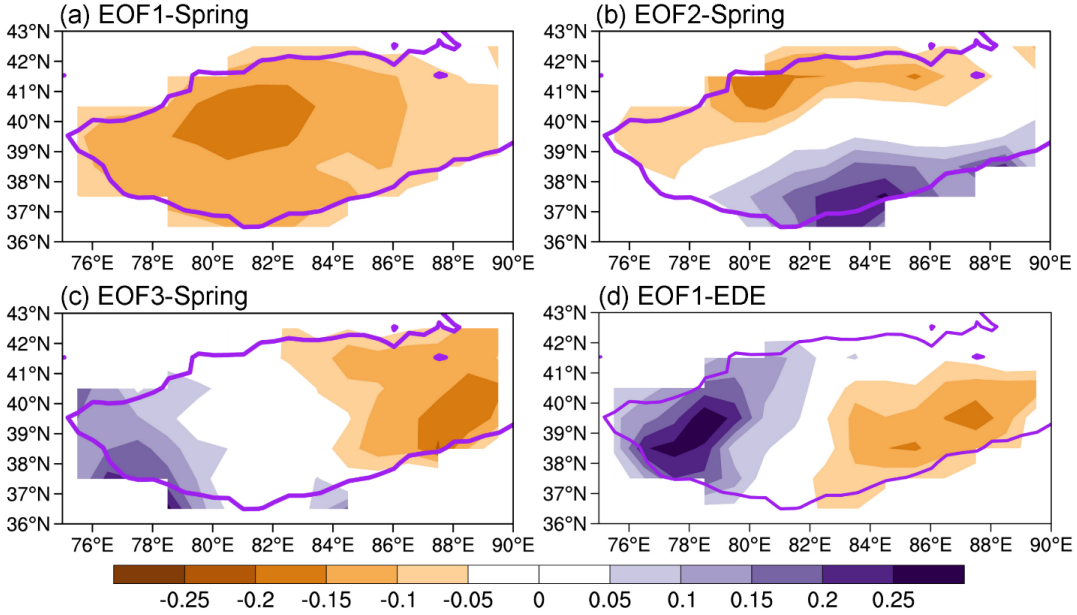


Figure 10. (a) The first, (b) the second, and (c) the third EOF modes of spring DOD derived from MODIS in TD from 2000 to 2025. (d) The first EOF mode of DOD during EDEs in TD from 2000 to 2025. The purple solid curve denotes the topographic contour line of 2000 m, representing the TD domain. The first three EOF modes of spring DOD are statistically significant and independent according to the test criteria of North et al. (1982).

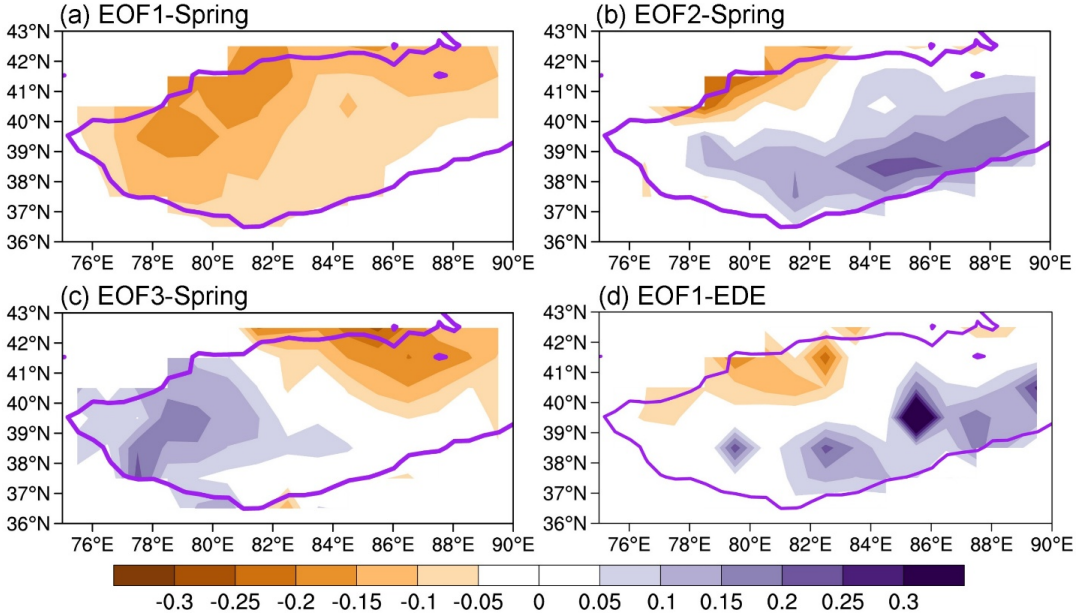


Figure 11. Same as in Fig. 10, but for DOD derived from IASI during 20008-2023.

https://doi.org/10.5194/egusphere-2026-6188
Preprint. Discussion started: 6 November 2026
© Author(s) 2026. CC BY 4.0 License.

Finally, based on CMIP6 simulations, the relationship between future extreme dust intensity and spring dust intensity in TD was briefly analyzed. Among the five numerical models capable of providing daily AOD, only the UKESM1-0 model could reproduce the historical inconsistency between the interannual variations of extreme dust intensity and spring dust intensity (Fig. 12a). The future projections from this model indicate under high-emission scenarios, significant differences in interannual variations of extreme dust intensity and spring dust intensity persist (Fig. 12b), whereas appropriate emission reductions would strengthen their correlations (Fig. 12c).

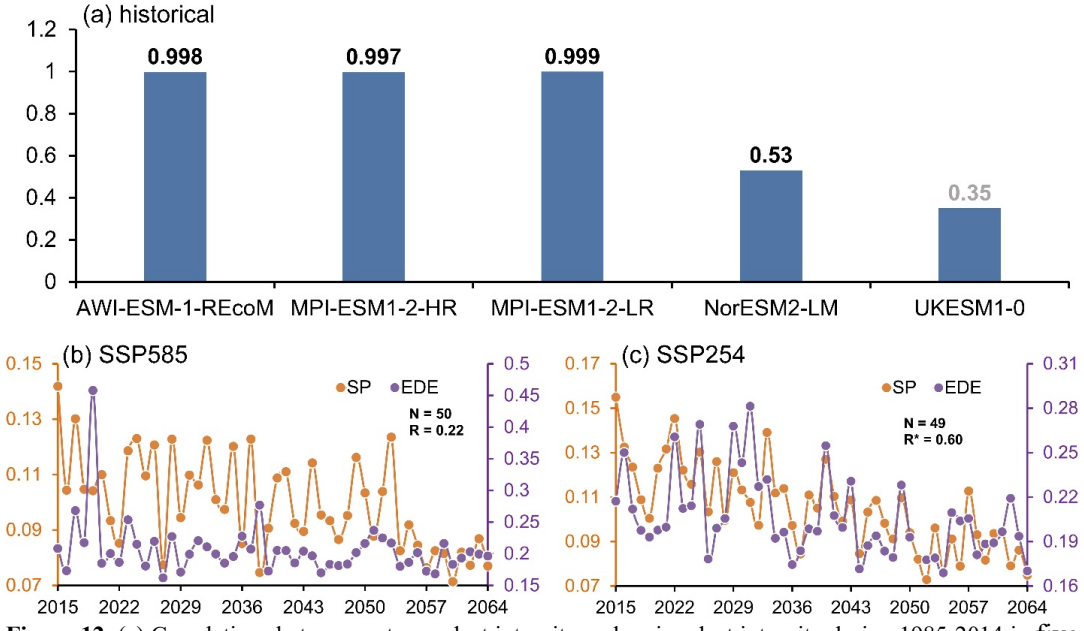


Figure 12. (a) Correlations between extreme dust intensity and spring dust intensity during 1985-2014 in five CMIP6 models. Black numbers indicate the correlation coefficients are significant at the 95% confidence level; gray numbers indicate the correlation coefficients are insignificant at the 95% confidence level. Time series of spring AOD and EDE AOD in TD during 2015-2064 derived from UKESM1-0 under (b) SSP585 and (c) SSP245. N represents the number of years in which EDE occurred, R represents the correlation coefficient, and label * indicates the correlation coefficient is significant at the 95% confidence level.

5. Conclusion and Discussion

Based on MODIS and IASI observations, this study investigated the interannual relationship between spring DOD and EDE DOD. The results reveal regional differences in the association between them: EDE DOD correlates significantly positively with spring DOD in NA and ME, while no significant correlation exists in TD. This phenomenon holds consistently in MODIS and IASI and is insensitive to different EDE thresholds (90th/85th percentile), which indicates a unique variability characteristic of EDE DOD in TD.

https://doi.org/10.5194/egusphere-2026-6188
Preprint. Discussion started: 6 November 2026
© Author(s) 2026. CC BY 4.0 License.

This decoupling in TD originates from inconsistent interannual low-level winds for spring DOD and EDE DOD, which are forced by separate large-scale circulations: spring winds by European precipitation anomalies and EDE winds by North Atlantic precipitation dipoles. Additionally, EOF analysis indicated the dominant mode of EDE DOD in TD aligned with the third mode of spring DOD. Since the third mode is significantly independent of the first mode of spring DOD which represents the spring-averaged pattern, the result further supports the relative independence of their spatiotemporal distributions.

Our study systematically analyzed EDEs in major dust-contributing regions and revealed EDEs in TD were influenced by specific circulations, rather than simply being an amplification of the dust background in spring. This finding emphasized the driving mechanisms of extreme weather events may be independent of seasonal conditions, particularly in regions regulated by complex teleconnections. The Gc-index constructed in this study integrated circulation signals from spring and EDEs, providing a physical basis for interannual predictions of EDE intensity in TD. In the future, it is still necessary to further integrate multi-source observations and advanced climate models to better encapsulate the complexity of dust activities, thereby improving the predictability of such high-impact events.

Although this study utilized quality-controlled satellite data, inherent satellite limitations may cause aerosol-cloud misclassification and bring some uncertainties to our conclusions. In the future, this issue could be addressed by combining satellite and ground-based observations and using machine learning or artificial intelligence to obtain more accurate aerosol datasets. In addition, limited daily AOD outputs from CMIP6 models restrict our future projection analysis, and small model sample sizes may also introduce uncertainties.

Data Availability

MODIS observations were downloaded from https://ladsweb.modaps.eosdis.nasa.gov/archive/allData/61/MOD04_L2. IASI observations were downloaded from https://doi.org/10.24381/cds.239d815c. ERA5 reanalysis data were obtained from https://doi.org/10.24381/cds.bd0915c6 and https://doi.org/10.24381/cds.adbb2d47. NCEP reanalysis data were obtained from https://downloads.psl.noaa.gov/Datasets/ncep.reanalysis2/Dailies/pressure/. The NDVI data were obtained from https://www.ncei.noaa.gov/data/land-normalized-difference-vegetation-index/access/. Linear Baroclinic Model is available at https://ccsr.aori.u-tokyo.ac.jp/~lbm/sub/lbm.html.

https://doi.org/10.5194/egusphere-2026-6188
Preprint. Discussion started: 6 November 2026
© Author(s) 2026. CC BY 4.0 License.

Author contribution

CZ and QZ designed the study and developed the overarching research goals and aims. QZ carried the study out and wrote the first draft with contributions from all co-authors. CZ and QZ processed the data with the assistance of ZC, XY, AM, FY, WH, and YW. CZ and QZ assumed oversight and leadership responsibility for the research activity planning and execution. All authors contributed to the improvement of results and revised the final paper.

Competing interests

The authors declare that they have no conflict of interest.

Financial support

This work was jointly supported by the Tianshan Young Talent Support Program of Xinjiang Uygur Autonomous Region (2024TSYCCX0044), National Natural Science Foundation of China (42505178), Shandong Provincial Natural Science Foundation (ZR2023QD169), Major Science and Technology Program of Xinjiang Uygur Autonomous Region (2024A03006-1), Natural Science Foundation of Xinjiang Uygur Autonomous Region (2022D01A366), Youth Innovation Team of China Meteorological Administration (CMA2024QN13), Scientific and Technological Innovation Team (Tianshan Innovation Team) project (2022TSYCTD0007), S&T Development Fund of CAMS (2021KJ034), and the third batch of the Tianchi Talent Introduction Program in Xinjiang Uygur Autonomous Region (2025).

References:

Bevacqua, E., Suarez Gutierrez, L., Jézéquel, A., Lehner, F., Vrac, M., Yiou, P., and Zscheischler, J.: Advancing research on compound weather and climate events via large ensemble model simulations, Nat. Commun., 14, 2145, https://doi.org/10.1038/s41467-023-37847-5, 2023.

Blumstein, D., Chalon, G., Carlier, T., Buil, C., Hebert, P., Maciaszek, T., Ponce, G., Phulpin, T., Tournier, B., Simeoni, D., Astruc, P., Clauss, A., Kayal, G., Jegou, R.: IASI instrument: technical overview and measured performances, in: Proceedings of Infrared Spaceborne Remote Sensing XII, SPIE, vol. 5543, SPIE, Bellingham, WA, 5543, https://doi.org/10.1117/12.560907, 2004.

Cañadillas Ramallo, D., Moutaoikil, A., Shephard, L. E., and Guerrero Lemus, R.: The influence of extreme dust events in the current and future 100 % renewable power scenarios in Tenerife, Renew. Energ., 184, 948-959, https://doi.org/10.1016/j.renene.2021.12.013, 2022.

Capelle, V., Chédin, A., Pondrom, M., Crevoisier, C., Armante, R., Crepeau, L., and Scott, N.A.: Infrared dust aerosol optical depth retrieved daily from IASI and comparison with AERONET

https://doi.org/10.5194/egusphere-2026-6188
Preprint. Discussion started: 6 November 2026
© Author(s) 2026. CC BY 4.0 License.



over the period 2007–2016, Remote Sens. Environ., 206, 15 32, https://doi.org/10.1016/j.rse.2017.12.008, 2018.

Chen, S., Zhao, D., Huang, J., He, J., Chen, Y., Chen, J., Bi, H., Lou, G., Du, S., Zhang, Y., and Yang, F.: Mongolia Contributed more than 42% of the Dust Concentrations in Northern China in March and April 2023, Adv. Atmos. Sci., 40, 1549-1557, https://doi.org/10.1007/s00376-023-3062-1, 2023.

Chen, Y., Chen, S., Bi, H., Zhou, J., and Zhang, Y.: Where is the Dust source of 2023 several Severe Dust events in China?, Bull. Am. Meteorol. Soc., 105, E2085-E2096, https://doi.org/10.1175/BAMS-D-23-0121.1, 2024.

Fu, Z. H., Zhou, W., Xie, S. P., Zhang, R., and Wang, X.: Dynamic pathway linking Pakistan flooding to East Asian heatwaves, Sci. Adv., 10, eadk9250, https://doi.org/10.1126/sciadv.adk9250, 2024.

Gandham, H., Dasari, H.P., Karumuri, A., Ravuri, P.M.K., and Hoteit, I.: Three dimensional structure and transport pathways of dust aerosols over West Asia, npj Clim. Atmos. Sci., 5, 45, https://doi.org/10.1038/s41612-022-00266-2, 2022.

Gui, K., Yao, W., Che, H., An, L., Zheng, Y., Li, L., Zhao, H., Zhang, L., Zhong, J., Wang, Y., and Zhang, X.: Record breaking dust loading during two mega dust storm events over northern China in March 2021: aerosol optical and radiative properties and meteorological drivers, Atmos. Chem. Phys., 22, 7905-7932, https://doi.org/10.5194/acp-22-7905-2022, 2022.

Huang, H., Zhu, Z., and Li, J.: Disentangling the unprecedented Yangtze River Basin extreme high temperatures in summer 2022: combined impacts of the reintensified La Niña and strong positive NAO, J. Clim., 37, 927-942, https://doi.org/10.1175/JCLI-D-23-0466.1, 2024.

Kataoka, T., Masson, S., Izumo, T., Tozuka, T., and Yamagata, T.: Can Ningaloo Niño/Niña develop without El Niño Southern Oscillation?, Geophys. Res. Lett., 45, 7040-7048, https://doi.org/10.1029/2018GL078188, 2018.

Kawai, K., Matsui, H., and Tobo, Y.: High potential of Asian dust to act as ice nucleating particles in mixed phase clouds simulated with a global aerosol climate model, J. Geophys. Res. Atmos., 126, https://doi.org/10.1029/2020JD034263, 2021.

Lei, H., Ma, Q., Chang, Y., Gu, Y., Wan, S., Zhu, Z., and Feng, G.: Multiscale interactions driving summer extreme precipitation in Central Asia, Geophys. Res. Lett., 51, e2024GL108882, https://doi.org/10.1029/2024GL108882, 2024.

Li, X., and Ginoux, P.: An Empirical Parameterization to Separate Coarse and Fine Mode Aerosol Optical Depth Over Land, Geophys Res Lett, 52, https://doi.org/10.1029/2024GL114397, 2025.

Liao, Z., Chen, Y., Li, W., and Zhai, P.: Growing threats from unprecedented sequential flood hot extremes across China, Geophys. Res. Lett., 48, https://doi.org/10.1029/2021gl094505, 2021.

Merdji, A.B., Lu, C., Xu, X., and Mhawish, A.: Long term three dimensional distribution and transport of Saharan dust: observation from CALIPSO, MODIS, and reanalysis data, Atmos. Res., 286, 106658, https://doi.org/10.1016/j.atmosres.2023.106658, 2023.

https://doi.org/10.5194/egusphere-2026-6188
Preprint. Discussion started: 6 November 2026
© Author(s) 2026. CC BY 4.0 License.



Mostamandi, S., Ukhov, A., Engelbrecht, J., Shevchenko, I., Osipov, S., and Stenchikov, G.: Fine and coarse dust effects on radiative forcing, mass deposition, and solar devices over the Middle East, J. Geophys. Res. Atmos., 128, e2023JD039479, https://doi.org/10.1029/2023JD039479, 2023.

Mu, F.F., and Fiedler, S.: How much do atmospheric depressions and Mongolian cyclones contribute to spring dust activities in East Asia?, npj Clim. Atmos. Sci., 8, 51, https://doi.org/10.1038/s41612-025-00929-w, 2025.

North, G.R., Bell, T.L., Cahalan, R.F., and Moeng, F.J.: Sampling errors in the estimation of empirical orthogonal functions, Mon. Weather Rev., 110, 699 706, https://doi.org/10.1175/1520 0493(1982)110<0699:SEITEO>2.0.CO;2, 1982.

Pons, F., Alberti, T., Messori, G., Dulac, F., and Faranda, D.: Assessing climate change impacts on the March 2024 compound floods and Saharan dust outbreak in Europe, J. Geophys. Res Atmos., 130, e2024JD042218, https://doi.org/10.1029/2024JD042218, 2025.

Pu, B., and Ginoux, P.: How reliable are CMIP5 models in simulating dust optical depth?, Atmos. Chem. Phys., 18, 12491-12510, https://doi.org/10.5194/acp-18-12491-2018, 2018.

Pu, B., and Jin, Q.: A record breaking trans Atlantic African dust plume associated with atmospheric circulation extremes in June 2020, Bull. Am. Meteorol. Soc., 102, E1340-E1356, https://doi.org/10.1175/BAMS-D-21-0014.1, 2021.

Rodríguez, S., and López Darias, J.: Emerging extreme Saharan dust events expand northward over the Atlantic and Europe prompting record breaking PM10 and PM2.5 episodes, Atmos. Chem. Phys., 24, 12031-12053, https://doi.org/10.5194/acp-24-12031-2024, 2024.

Shi, J., Huang, H., Fedorov, A.V., Holbrook, N.J., Zhang, Y., and Ding, R.: Northeast Pacific warm blobs sustained via extratropical atmospheric teleconnections, Nat. Commun., 15, 2832, https://doi.org/10.1038/s41467-024-47032-x, 2024.

Singh, C., Singh, S.K., Chauhan, P., and Budakoti, S.: Simulation of an extreme dust episode using WRF CHEM based on optimal ensemble approach, Atmos. Res., 249, 105296, https://doi.org/10.1016/j.atmosres.2020.105296, 2021.

Takaya, K., and Nakamura, H.: A formulation of a phase independent wave activity flux for stationary and migratory quasigeostrophic eddies on a zonally varying basic flow, J. Atmos. Sci., 58, 608-627, https://doi.org/10.1175/1520 0469(2001)058<0608:AFOAPI>2.0.CO;2, 2001.

Urraca, R., Cappucci, F., Lanconelli, C., and Gobron, N.: Assessing discrepancies in global aerosol trends from satellites, models and reanalyses, Remote Sens. Environ., 328, 114827, https://doi.org/10.1016/j.rse.2025.114827, 2025.

Watanabe, M., and Kimoto, M.: Atmosphere ocean thermal coupling in the North Atlantic: A positive feedback, Q. J. R. Meteorol. Soc., 126, 3343-3369, https://doi.org/10.1002/qj.49712657017, 2000.

Wei, J., Wang, Z., Li, Z., Li, Z., Pang, S., and Xi, X.: Global aerosol retrieval over land from Landsat imagery integrating transformer and Google earth engine, Remote Sens. Environ., 315, 114404, https://doi.org/10.1016/j.rse.2024.114404, 2024.

https://doi.org/10.5194/egusphere-2026-6188
Preprint. Discussion started: 6 November 2026
© Author(s) 2026. CC BY 4.0 License.



Wu, H.J., Lu, H.Y., Wang, J.J., Chen, Y., and Cui, M.C.: A new estimate of global desert area and quantity of dust emission, Chin. Sci. Bull., 67, 860-871, https://doi.org/10.1360/TB-2021-1215, 2022.

Xue, Y., Zhang, X., Lei, J., Li, S., Liu, L., Wang, Z., Tian, W., Tang, X., and Chen, X.: East Asian dust storm in March 2021: Perspective views from ground observation, satellite measurement and numerical simulation, Atmos. Environ., 350, 121152, https://doi.org/10.1016/j.atmosenv.2025.121152, 2025.

Yanai, M., Esbensen, S., and Chu, J.: Determination of Bulk Properties of Tropical Cloud Clusters from Large Scale Heat and Moisture Budgets, J. Atmos. Sci., 30, 611-627, https://doi.org/10.1175/1520 0469(1973)030<0611:DOBPOT>2.0.CO;2, 1973.

Yin, Z., Wan, Y., Zhang, Y., and Wang, H.: Why super sandstorm 2021 in North China?, Natl. Sci. Rev., 9, https://doi.org/10.1093/nsr/nwab165, 2022.

Zamora, L. M., and Kahn, R. A.: First observational evidence that dust driven cloud phase changes cool the surface over summertime Arctic sea ice, Geophys. Res. Lett., 51, e2024GL110423, https://doi.org/10.1029/2024GL110423, 2024.

Zhu, Q., and Liu, Y.: The dominant factor in extreme dust events over the Gobi Desert is shifting from extreme winds to extreme droughts, npj Clim. Atmos. Sci., 7, https://doi.org/10.1038/s41612-024-00689-z, 2024.

Zittis, G., Almazroui, M., Alpert, P., Ciais, P., Cramer, W., Dahdal, Y., Fnais, M., Francis, D., Hadjinicolaou, P., Howari, F., Jrrar, A., Kaskaoutis, D.G., Kulmala, M., Lazoglou, G., Mihalopoulos, N., Lin, X., Rudich, Y., Sciare, J., Stenchikov, G., Xoplaki, E., and Lelieveld, J.: Climate change and weather extremes in the eastern mediterranean and Middle East, Rev. Geophys., 60, e2021RG000762, https://doi.org/10.1029/2021RG000762, 2022.